Taylor & Francis
Taylor & Francis Group

Journal of Adhesion Science and Technology

ISSN: (Print) (Online) Journal homepage: https://www.tandfonline.com/loi/tast20

Low-speed bending impact behaviour of adhesively bonded dissimilar single-lap joints

M. Gokhan Atahan & M. Kemal Apalak

To cite this article: M. Gokhan Atahan & M. Kemal Apalak (2021): Low-speed bending impact behaviour of adhesively bonded dissimilar single-lap joints, Journal of Adhesion Science and Technology, DOI: 10.1080/01694243.2021.1987720

To link to this article: https://doi.org/10.1080/01694243.2021.1987720

JOURNAL OF ADHESION SCIENCE AND TECHNOLOGY
https://doi.org/10.1080/01694243.2021.1987720

Low-speed bending impact behaviour of adhesively bonded dissimilar single-lap joints

M. Gokhan Atahan[a] and M. Kemal Apalak[b]

[a]Department of Mechanical Engineering, Abdullah Gul University, Kayseri, Turkey; [b]Department of Mechanical Engineering, Erciyes University, Kayseri, Turkey

ABSTRACT

This study investigates the low-speed bending impact behaviour of adhesively bonded dissimilar single-lap joints and the effects of both strength and plastic deformation capability of adherend material on adhesive failure. Dissimilar adhesive single-lap joint specimens, such as Al 2024-T3 (top adherend)-Al 5754-0 (bottom) and Al 5754-0 (top)-Al 2024-T3 (bottom), were tested at two impact energy levels (3 and 11 J) for two overlap lengths (25 and 40 mm). The progressive failure analysis of the adhesive layer was also conducted by the non-linear explicit finite element method. The adhesive layer was modelled with a 3D cohesive layer along with the upper and lower adhesive interfaces and a non-linear continuum adhesive region between two cohesive layers. The continuum adhesive region had elasto-plastic adhesive properties whilst the cohesive layers obeyed 3D cohesive rules. The experimental and predicted contact force-time, contact force-displacement diagrams, axial separation lengths of the failed adhesive region, permanent deflection of the bonded region, fracture surfaces were in good agreement. The strength and plastic deformation capability of adherend materials and impact energy levels affected the progressive adhesive failure behaviour. The proposed finite element model was successful reasonably in predicting the initiation and propagation of the adhesive failure.

ARTICLE HISTORY
Received 23 April 2021
Revised 13 September 2021
Accepted 17 September 2021

KEYWORDS
Low-speed impact; cohesive zone model; adhesive failure; single-lap joint; adhesive joint; progressive failure analysis; dissimilar joint

1. Introduction

Adhesive joints can serve under static and dynamic loads as well as thermal loads [1–5]. However, the engineering materials exhibit rather different stress and deformation behaviours under impulsive loads than those under static loads. The stress and deformation states, the strength of adhesive joints are not still well-known for various impact loadings and need detailed experimental and theoretical studies [6].

Higuchi et al. [7] investigated the stress wave propagation and temporal stress distributions of adhesive single-lap joints under a tensile impact loading based on an elastic three-dimensional finite element analysis. The maximum stresses occurred near the

CONTACT M. Kemal Apalak apalakmk@erciyes.edu.tr Department of Mechanical Engineering, Erciyes University, Kayseri, Turkey.

edge of the interface and increased as the overlap length and adhesive thickness increased and the adherend thickness decreased. Sawa et al. [8] analyzed the stress variations in butt adhesive joints of dissimilar hollow cylinders under tensile impact loading using the finite element method to determine the effects of different Young's modulus of dissimilar adherends and adhesive thickness on the stress variations at the interfaces. The maximum principal stress in the lower interface decreased as the adhesive thickness increased, and the stress variations of similar and dissimilar adhesive joints were different. Higuchi et al. [9] studied stress wave propagation and stress distribution in adhesive butt joints of similar T-shaped under bending impact moment using a three-dimensional finite element method and determined the effects of Young's modulus of adherends, adhesive thickness, and the web length of T-shaped adherends on the stress wave propagation. The maximum principal stress in adhesive-adherend interfaces increased as Young's modulus of adherends increased and the adherend thickness decreased. Vaidya et al. [10] investigated the low-speed impact behaviour of an adhesively bonded single-lap joint under a transverse normal impact load. They simulated the adhesive failure using a cohesive failure model based on ultimate failure strain. Their experimental and numerical studies indicated that the peel stresses increased since the adhesively bonded single-lap joint experienced a considerable deflection under a transverse load, and an asymmetric stress distribution occurred in the adhesive layer.

Yildirim and Apalak [11] investigated the transverse low speed impact behaviour of adhesively bonded similar (Al–Al and St–St) and dissimilar (Al–St and St–Al) clamped plates using the explicit finite element method. They presented the contact force and plastic dissipation variations for different impactor mass and radius values and impact energies. They showed that the damage areas in the adhesive layer were minimal in adhesively bonded Al–Al plates having better plastic deformation capability, whereas they were maximal for stiffer adhesively bonded St–St plates. Liao et al. [12] studied the stress wave propagations and interface stress distributions of the adhesive single-lap joint made of dissimilar adherends under tensile impact loads. The strength of the similar adhesive joints was higher than those of the dissimilar adhesive joints.

Asgharifar et al. [13] investigated the effects of adhesive thickness, the solid impactor size, and its velocity, the mechanical properties of adhesive and strain-rate effect on the transient stress distributions of adhesively bonded single-lap joints under an impact loading using the three-dimensional explicit finite element method. The adhesive layer experienced lower stresses in case of a smaller impactor, a lower impact velocity, a lower adhesive modulus, and a thicker adhesive layer. Yildirim and Apalak [14] also conducted an experimental study on the low-speed impact behaviour of adhesively bonded similar (Al–Al and St–St) and dissimilar (Al–St and St–Al) plates. The bonded Al–Al plates having better plastic deformation capability dissipated more impact energy than the bonded stiffer St–St plates. The plate stiffness had an important role in the deflections of bonded plates, contact durations, contact force levels, and adhesive failure surfaces. Sankar et al. [15] investigated the effect of similar and dissimilar adherends on the dynamic strength of single-lap joints using the split Hopkinson pressure bar technique for steel and aluminium adherends and Araldite® 2014. The adhesive joints exhibited different dynamic strengths depending on both

adherend material and its combination. The steel-steel joints had higher strength than the aluminium–aluminium joints. The combination of adherend materials was concluded to be important for joint design.

Atahan and Apalak [16,17] investigated the low-speed bending and oblique impact behaviours of adhesively bonded similar aluminium single-lap joints for different overlap lengths and impact energies. They also implemented a cohesive zone model to predict adherend-adhesive interfacial failure and a continuum model for adhesive failure through the adhesive region between interfaces. The adhesive failures initiated at one free edge of the upper adherend-adhesive interface and propagated along with this interface after it advanced through the adhesive thickness towards the other interface and returned. The adhesive plasticity allowed more energy dissipation, and the overlap length, impact energy levels played an important role in the progressive adhesive failure. Lower peak contact forces, shorter contact durations, and earlier damage initiation and propagation through the adhesive layer were observed with increasing oblique impact angles.

Boling and Dongyun [18] investigated the effects of adhesive thickness and overlap length, projectile size, and velocity, and adhesive strain-rate value on the transient stress distributions in an adhesively bonded composite-titanium single-lap joint under an impact loading considering the progressive failure properties of composite adherends. The peak adhesive stresses are reduced with increasing adhesive thickness and overlap length and reducing the projectile diameter and impact velocity. The dynamic response of the adhesive layer at different strain rates exhibited a dependency on loading speed and adhesive mechanical properties. Thus, the strain rate effect on the stress-strain curves was negligible for high modulus adhesives under low loading speeds.

Machado et al. [19] investigated the mechanical behaviour of mixed adhesive single-lap joints under quasi-static and impact loads. They modified cohesive laws with the experimental data obtained at different strain rates to predict the mechanical behaviours of various types of mixed adhesive joints bonded with stiffer adhesives. Their models were less effective for joints having high-ductility adhesives under an impact load. Jia et al. [20] determined the shear properties of polyurethane adhesives at room and low temperatures for different loading rates using thick adherend shear test specimens. The shear strength of polyurethane adhesive reduced as the temperature decreased in quasi-static conditions. The adhesive shear strength increased with increasing loading speed. However, the adhesive shear strength at room temperature under quasi-static conditions was not suitable for both design and analysis of adhesive joints at low temperatures under impact loadings. Jia et al. [21] tested the cohesive parameters of a polyurethane adhesive under different strain rate conditions. The cohesive properties of the adhesive were different under impact loads. Therefore, they offered a weighted average strain rate method to determine the effective strain rate of the adhesive under the high strain rate condition and developed a strain rate-dependent cohesive constitutive model of the adhesive. After their model was calibrated by experimental data, the impact tensile shear tests of composite single-lap joints were performed at high loading speeds, and their model was implemented to finite element analysis. Their method was reasonably successful in the determination of strain rate dependent-cohesive parameters. Yildiz et al. [22] determined the displacement fields in

fully bonded aluminium circular plates subjected to shock wave loadings by digital image correlation techniques. They also implemented experimental high strain responses of the adhesive layer to a finite element model to examine the effect of adhesive thickness and Young's modulus on the responses of bonded adhesive plates under shock wave loadings. The bonded plate was less deformed and absorbed less energy with increasing adhesive thickness and adhesive modulus.

In general, the adhesively bonded butt and single-lap joints are used to determine the dynamic response of the adhesive materials under an impact load. The impact energy level and impulsive load are more effective on the strain distribution and deformation speed for the adhesive material. Therefore, the adhesive material can deform at low, moderate, high speeds by exhibiting different strain and stress responses depending on the strain rate. However, a brittle or ductile adhesive composition has a different deformation response, such as sudden failure at a low failure strain level or plastic deformation and dissipation with a high failure strain. In addition, the plastic deformation capability of the adherend materials can affect adhesive deformations; thus, a ductile adherend can dissipate most of the impact energy whilst an adherend with high stiffness and strength can accumulate and restore elastically impact energy. Consequently, the range of the impact energy, impact velocity, the duration of the impulsive load, and the individual mechanical responses of the adhesive and adherend materials need to be determined with suitable stress analysis.

This study investigates the effects of aluminium adherends having different plastic deformation capability and strength, impact energy and overlap length on both the progressive adhesive failure and the dynamic bending response of adhesive single-lap joint under low-speed impact conditions. An experimental programme and an explicit finite element analysis were performed simultaneously. A 3D cohesive adhesive model along with the adherend-adhesive interfaces, a 3D elasto-plastic continuum model for the adhesive region between two adhesive interfaces, linear degradation algorithms were implemented to predict both the initiation and propagation of adhesive failure. The contact force-time, contact force-transverse displacement diagrams, fracture surfaces, progressive adhesive failure (axial length and separation width) were discussed in detail based on the experimental and explicit finite element analyses. The results were also compared with the low-speed impact behaviour of adhesively bonded single-lap joints with similar adherends [16].

2. Low-speed impact tests

The low-speed impact tests of adhesively bonded dissimilar single-lap joints were carried out in order to determine the effects of the plastic deformation capability and strength of adherends on the low-speed bending impact behaviour of an adhesively bonded single-lap joint. The adhesive joints were prepared as two configurations, such as (i) the top adherend (Al 2024)—the bottom adherend (Al 5754) and (ii) the top adherend (Al 5754)—the bottom adherend (Al 2024). The aluminium adherends were cut in a thickness of 2 mm, a width of 25 mm, in lengths of 112.5 and 120 mm. The effective length L of adhesive joints was kept constant at 160 mm for the overlap lengths b of 25 and 40 mm. The adhesive joint, dimensions, boundary conditions, and

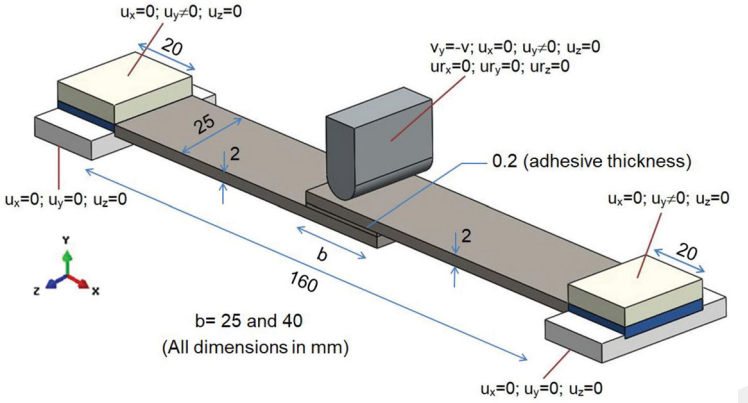

Figure 1. The dimensions and boundary conditions of an adhesively bonded single-lap joint.

impactor geometry were shown in Figure 1. The aluminium adherends were bonded by Araldite® 2015 adhesive suitable for impact loads [23]. The adherend surfaces were cleaned suitably and bonded by applying a low pressure in an apparatus designed for bonding purposes, and the specimens were left to an average curing period of 72 h at room temperature. The adhesive thickness for all specimens was kept at 0.2 mm as possible using four washers with a thickness of 4.2 mm in the bonding apparatus. A liquid paraffin layer was applied to the internal surfaces of the bonding apparatus to avoid bonding between adherends and apparatus surfaces. The low-speed impact tests were performed *via* Fractovis Plus impact test machine using a semi-cylindrical impactor with a mass of 5.302 kg, a nose radius of 5 mm, and a width of 25 mm (Figure 2). The load cell of the impactor has a sampling frequency range of 1–2000 kHz. The impact load measurement limit of the impactor is 41.020 kN. During the impact tests, the sampling frequency was selected 250 kHz and the sampling points of 10,000 were used for each impact test depending on the contact period. All impact tests were repeated at least twice for average impact velocities of 1.064 and 2.037 m/s corresponding to the impact energies E of 3 and 11 J, respectively. After the impact tests, the experimental contact force-time and contact force-displacement diagrams were prepared and compared with the diagrams obtained from the explicit finite element analysis. In addition, the fully and partly separated fracture surfaces were examined using macroscope and scanning electron microscopy (SEM), and the permanent transverse central displacements and axial separation lengths were measured.

3. Finite element modelling

During the impact tests, it is a very difficult task to visualize simultaneously the initiation and propagation of the three-dimensional adhesive failure. To investigate the effects of impact energy, overlap length, and the plastic deformation capability and strength of the adherend materials, as well as the adhesive material on the progressive adhesive failure behaviour the three dimensional explicit finite element analyses of the adhesively bonded single-lap joints, were performed in the test impact conditions using ABAQUS/Explicit software [24].

Figure 2. Fractovis Plus impact test machine and components.

The left and right holders were modelled as blocks made of steel with high strength in a length of 20 mm (Figure 1). In the preliminary analyses they were assumed to have elasto-plastic material behaviour, but serious plastic deformations which affect the general deformation and stress states of the adhesive joints, were not observed in these steel blocks; therefore, during the main analyses they were modelled as elastic materials to speed up calculations. The holder regions were meshed using a 3 D continuum finite element C3D8R with three degrees of freedom at each node using the reduced integration method. A pressure of 20 bar was applied to the adherend surfaces contacting these holders as in the impact test equipment. The top holders can move only along the y-direction whereas the bottom holders are completely fixed. A friction coefficient of 0.5 was set between the holders and contact surfaces of the specimen. Due to the damage evaluation in the cohesive zone based on the failure characteristics of adhesive material, the damaged cohesive elements were automatically removed. As a result, the adherend and inter adhesive surfaces contacting with the cohesive zones may become free and contact each other. The general contact algorithm can cope with successfully these dynamically occurring probable contact states between the impactor, specimens, and holders.

The actual impactor has semi-cylindrical tip geometry with a radius of 5 mm, its geometry was modelled as a rigid shell region with a DISCRETE RIGID definition, and meshed with a finite element type R3D4 which is suitable for shell geometry. The degree of freedoms (displacements and rotations) of the impactor part was specified by defining a reference point inside the impactor. An impactor mass of 5.302 kg was also defined *via* this reference point. The displacement component along only the y-direction was free, the other displacement and rotation components were set to zero. The general contact algorithm was also defined between the impactor outer surface and the outer surfaces of the adhesive joint, and a friction coefficient of 0.25 was specified. An initial velocity of 1.064 or 2.037 m/s along the y-direction was set to this reference point depending on the impact energy level $E = 3$ or 11 J, respectively.

The adherends were produced from Al 2024-T3 with high strength and partially low ductility, and Al 5754-0 with low strength and high ductility to examine the effect of

adherend ductility on the adhesive failure (Table 1). The impact tests of adhesively bonded single-lap joints showed that both adherends underwent plastic deformations and the failure initiated at the free end of the upper adhesive interface and propagated mostly along with this interface. Therefore, both top and bottom adherends were modelled as elasto-plastic material using the measured stress-strain curves (Figures 3(a,b)) and a 3D continuum finite element C3D8R.

A 3D cohesive layer with an artificial thickness of 0.02 mm was placed along the top and bottom adhesive interfaces based on the cohesive zone model and meshed with a single cohesive element (COH3D8) through the interface thickness (Figure 4). The adhesive region in a thickness of 0.16 mm between these two cohesive layers was divided into four layers through-thickness and modelled using a 3 D continuum finite element C3D8R with elasto-plastic material behavior (Figure 3(c)). A failure strain of 0.17 and an absolute failure displacement of 0.065 mm were used for the middle adhesive region [11]. This approach considers the energy dissipation of the adhesive layer affecting the contact force level and

Table 1. Mechanical properties of Al 2024-T3 and Al 5754-0 [16].

Materials	Density (kg/m^3)	Modulus of elasticity (GPa)
Al 2024-T3	2780	73
Al 5754-0	2660	68

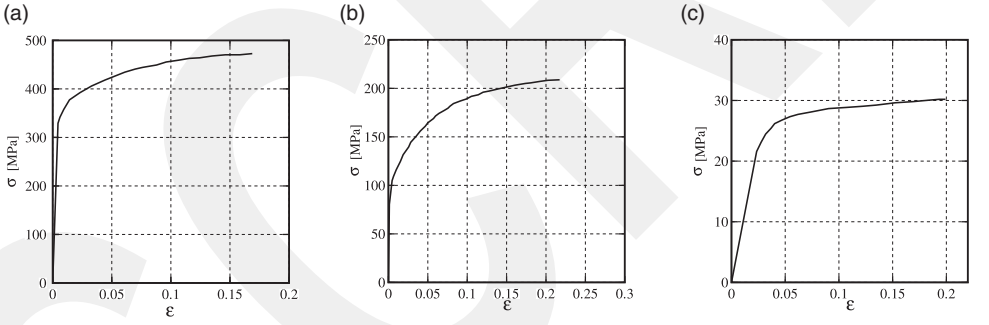

Figure 3. Stress–strain diagrams of (a) aluminium 2024-T3, (b) aluminium 5754-0, and (c) adhesive (Araldite® 2015) [11,16].

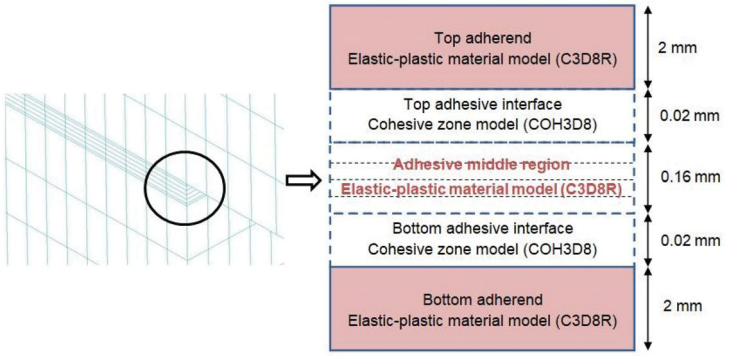

Figure 4. Numerical model of bonding region.

Table 2. Mechanical and cohesive properties of adhesive (Araldite® 2015) [26].

E GPa	G GPa	υ	t_n^o MPa	t_s^o MPa	t_t^o MPa	ρ kg/m^3
1.85	0.56	0.33	21.63	17.9	17.9	1400

contact durations. The maximum nominal stress criterion was used to predict damage initiation, and the measured failure displacement values of Araldite® 2015 were used to evaluate the adhesive damage propagation in the cohesive adhesive regions. The low-speed bending impact tests exhibit similar bending conditions to those under quasi-static loads. Therefore, the MMF (mixed mode flexure) tests involving mode I and II type failures of the adhesive material provide more appropriate measured displacement values for the damage response of adhesive under a bending moment. Wong [25] measured a failure displacement value of 0.065 mm with the MMF test for Araldite® 2015. In addition, Campilho et al. [26] measured the cohesive parameters of Araldite® 2015 from quasi-static tests. These mechanical properties and cohesive parameters are given in Table 2. After a local zone in cohesive regions was agreed to damage and the corresponding cohesive element was removed the remaining adherend and adhesive outer surfaces may contact each other. This state was also managed by applying the general contact algorithm to these surfaces.

The element deletion option was activated to observe the progressive adhesive failure. If any finite element satisfied the failure criteria, its mechanical properties were degraded gradually and their effects on the global stiffness matrix were reduced. As a result, this element become physically inactive but existed in the stiffness matrix. A refined mesh was generated using the BIAS command in the critical high stress and strain concentration regions. The 3D cohesive model for the regions between adherends and adhesive relies on a traction–separation relation and uses the maximum nominal stress criterion to predict the damage initiation. This criterion assumes that the damage initiates when the maximum nominal stress ratio reaches one value as follows

$$\max\left\{\frac{\langle t_n\rangle}{t_n^o}, \frac{t_s}{t_s^o}, \frac{t_t}{t_t^o}\right\} = 1 \tag{1}$$

where $\langle\ \rangle$ is Macaulay brackets, t_n^o, t_s^o, and t_t^o are normal and shear tractions, respectively. In case the damage is initiated the stress components at any integration point in the cohesive zone are assumed to be

$$t_n = (1-D)\bar{t}_n, \ \text{if}\ \bar{t}_n \geq 0 \tag{2}$$

$$t_n = \bar{t}_n, \ \text{if}\ \bar{t}_n \leq 0\ \ (\text{nodamage}) \tag{3}$$

$$t_s = (1-D)\bar{t}_s \tag{4}$$

$$t_t = (1-D)\bar{t}_t \tag{5}$$

where $\bar{t}_n$, $\bar{t}_s$, and $\bar{t}_t$ are predicted stress components based on the elastic traction-separation behaviour in case the damage has not yet occurred [24]. The effective interface separation δ_m can be defined as

$$\delta_m = \sqrt{\langle\delta_n\rangle^2 + {\delta_s}^2 + {\delta_t}^2} \tag{6}$$

where δ_n, δ_s, and δ_t are interfacial separations along with the normal, shear directions, respectively. The damage parameter D can be used for the damage evolution in terms of the effective separation δ_m based on the linear and exponential rules for the damage evolution as follows

$$D = \beta\,\frac{\delta_m^f}{\delta_m^{max}} \tag{7}$$

for the linear damage evolution

$$D = 1-\frac{\delta_m^o}{\delta_m^{max}}\left(1-\frac{1-\exp\left(-\alpha\,\beta\right)}{1-\exp\left(-\alpha\right)}\right) \tag{8}$$

for the exponential damage evolution, where

$$\beta = \frac{\delta_m^{max}-\delta_m^o}{\delta_m^f-\delta_m^o} \tag{9}$$

and α is a non-dimensional parameter, δ_m^o is effective interfacial separation at failure initiation, δ_m^f and δ_m^{max} is effective interfacial separation at failure and δ_m^{max} is maximum effective interfacial separation during the loading, respectively [24,27]. The evolution damage parameter α applies a linear effect for 0 and an exponential effect for a value towards 8. A linear softening rule was used for all specimen test conditions.

In the explicit finite element analysis, the outer surface of the impactor and the top surface of the upper adherend were matched each other and General Contact Algorithm was also defined for the interaction of these matched surfaces. As soon as these two surfaces have interacted the internal forces in the Cartesian coordinates were automatically calculated using stress components and were stored at a specified period in the analysis database. To provide the compatibility of both measured and calculated force histories the component of the calculated resultant force, which is coinciding with the load cell axis, was only considered.

4. Experimental and analysis

The experimental study addresses the effects of top and bottom adherend material combination, overlap length, and impact energy on the bending impact behavior of dissimilar adhesive single-lap joints were investigated. For this purpose, dissimilar adherend combinations [Al 2024 (T)op-Al 5754 (B)ottom, Al 5754 (T)-Al 2024 (B)], two

overlap lengths (25 and 40 mm), and two impact energy levels (3 and 11 J) were considered. The impact tests were repeated at least twice until the results were consistent. The dissimilar material combinations of adherends and overlap length may affect the adhesive damage mechanism and the overall load-bearing capability of adhesive joints. The adherend materials, such as Al 2024 and Al 5754 have different strength and plastic deformation capabilities; therefore, dissimilar adherend combinations (T 2024-B 5754 and T 5754-B 2024) were also compared with similar adherend combinations (T 2024-B 2024 and T 5754-B 5754) [16]. To determine the effects of different adherend strength and plastic deformation capability on the low speed bending impact behaviour of the adhesively bonded single-lap joints the contact force-time variation, the contact force-central transverse deflection variation, the adhesive separation length, the after-impact deformed geometry, the permanent central deflection, and the adhesive fracture surfaces were evaluated individually for each joint configuration. The explicit dynamic finite element analyses of the dissimilar adhesive single-lap joints were also carried out based on a combined cohesive zone and continuum model for the adhesive layer. Especially, the initiation and propagation through the adhesive layer were examined, and the predicted and experimental results were compared.

Figure 5 shows the effects of the impact energy level, overlap length, and adherend material combination on the contact force-time variations based on the experimental and numerical results for dissimilar adhesive single-lap joints. For an overlap length ($b = 25$ mm), the mechanical properties of the top and bottom adherends affect the peak contact force level and the total contact duration; thus, T 2024-B 5754 adhesive joint experiences lower contact forces than those of T 5754-B 2024 adhesive joint but shorter contact durations. The top adherend first encounters the impactor, and the strength and plastic deformation capability of the top adherend becomes apparent. A top 2024 adherend results in the contact force to increase due to its high strength and partly low plastic deformation capability. However, the presence of an Al 5754 adherend with low strength but better plastic deformation capability provides the impact energy to be dissipated by the Al 5754 adherend, and the contact force levels to reduce. However, the penetration time (t^p) and total contact time (t^t) change negligibly in comparison to the similar T 2024-B 2024 and T 5754-B 5754 adhesive joints (Table 3).

A top Al 5754 adherend contributes additionally to the reduction of contact force levels. The peak contact force levels for T 2024-B 2024 adhesive joint become highest whereas the peak contact force levels for T 5754-B 5754 adhesive joint are lowest among all joint configurations. A better plastic deformation capability for adherend material improves the dissipation of the applied impact energy and the contact force transferred to the adhesive joint by the impactor is also reduced reasonably. An adherend material with high strength results in the impact energy to be stored elastically; therefore, the adhesive layer experiences higher internal force distributions which may cause earlier damage initiation in the adhesive layer whilst the total contact duration is not affected evidently. The impact energy level affects both the contact force level and the total contact duration. However, the contact force variations exhibit apparent oscillations which indicate probable propagation of adhesive damage with increasing impact energy to $E = 11$ J. A higher impact energy results in a higher contact force level and

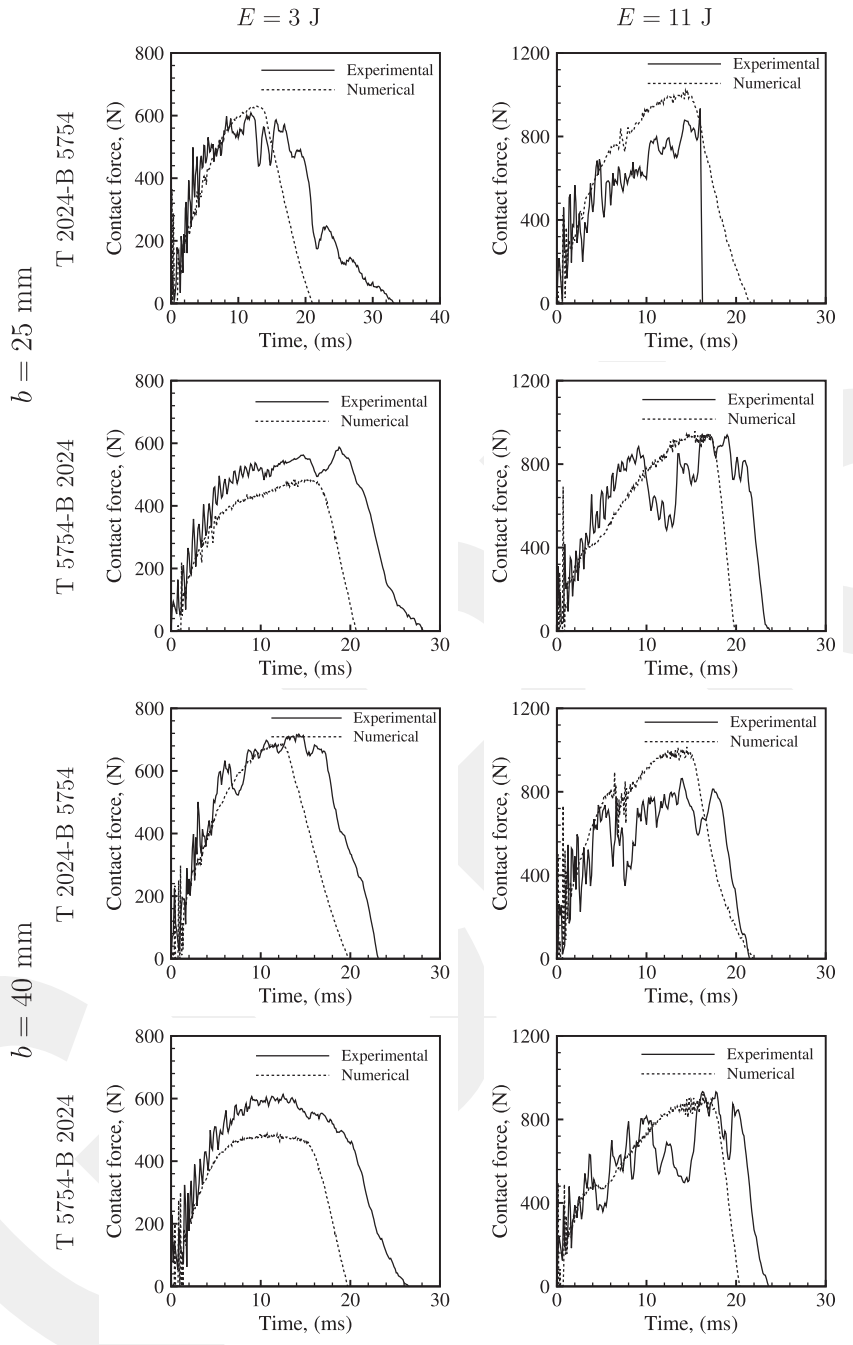

Figure 5. Experimental and numerical contact force-time diagrams for dissimilar adhesive single-lap joints ($b = 25$, 40 mm, $E = 3$, 11 J).

shorter contact duration (Figure 5, Table 3). The material combination and settlement of adherends still play an important role in the contact force levels and the contact duration.

Table 3. The experimental and numerical peak contact force (P_{max}), penetration time (t^p), total contact time (t^t), axial separation length (Δ), permanent central deflection (δ), plastic dissipation energy (E^d) values, and failure types for dissimilar and similar adhesive single-lap joints [16,17].

			P_{max} (N)		t^p (ms)		t^t (ms)		Δ (mm)		δ (mm)		E^d (J)		
E (J)	b (mm)	Joint	Exp	Num	Exp	Num	Exp	Num	Exp	Num	Exp	Num	Num	Failure type	Probable failure reasons
3	25	T 2024-B 5754	608.7	630.1	11.9	12.7	33.3	21.1	0.0	0.0	6.0	6.7	0.96	No	THSA 2024, OL, E
		T 5754-B 2024	587.6	484.9	18.8	15.7	28.4	20.8	12.0	13.2	14.0	9.7	1.18	Top interface	TLSA 5754, OL, E
		T 2024-B 2024	726.4	655.0	11.0	11.9	30.8	29.4	0.0	15.1	2.0	1.8	0.54	No	THSA 2024-BHSA 2024, OL, E
		T 5754-B 5754	538.6	448.5	11.6	16.3	26.1	21.1	10.0	12.8	12.0	10.4	1.39	Top interface	TLSA 5754-BLSA 5754, OL, E
	40	T 2024-B 5754	717.4	685.6	14.3	12.5	23.1	19.9	0.0	0.0	6.0	6.0	1.05	No	THSA 2024, OL, E
		T 5754-B 2024	613.2	488.6	12.5	10.5	26.5	19.7	18.0	15.8	13.0	8.6	1.20	Cohesive and top interface	TLSA 5754, OL, E
		T 2024-B 2024	786.0	633.9	6.0	12.2	32.5	29.7	18.0	23.2	4.0	1.4	0.64	Mixed	THSA 2024-BHSA 2024, OL, E
		T 5754-B 5754	591.2	491.0	18.1	11.5	27.8	19.4	17.0	12.2	13.0	9.2	1.38	Top interface	TLSA 5754-BLSA 5754, OL, E
11	25	T 2024-B 5754	933.8	1022.1	16.0	14.6	16.3	21.7	25.0	16.5	12.0	16.7	3.89	Cohesive	THSA 2024, OL, E
		T 5754-B 2024	940.8	957.8	16.8	15.4	23.8	19.9	17.0	14.6	25.0	21.2	3.38	Top interface	TLSA 5754, OL, E
		T 2024-B 2024	812.1	875.7	2.5	5.9	6.0	6.4	25.0	25.0	14.0	12.0	1.45	Cohesive and top interface	THSA 2024-BHSA 2024, OL, E
		T 5754-B 5754	658.8	914.4	18.5	17.0	23.3	21.2	18.0	17.0	27.0	23.3	3.55	Top interface	TLSA 5754-BLSA 5754, OL, E
	40	T 2024-B 5754	863.7	1015.1	14.0	14.5	21.5	21.9	21.0	23.8	17.0	16.0	4.26	Cohesive and top interface	THSA 2024, OL, E
		T 5754-B 2024	933.3	920.7	16.3	16.3	23.6	20.4	25.0	22.1	26.0	20.5	3.37	Top interface	TLSA 5754, OL, E
		T 2024-B 2024	1018.5	1097.1	16.0	13.2	24.4	17.5	40.0	27.0	14.0	16.7	3.78	Mixed	THSA 2024-BHSA 2024, OL, E
		T 5754-B 5754	947.9	877.7	16.0	18.0	22.0	21.3	20.0	23.7	23.0	22.3	3.54	Cohesive and top interface	TLSA 5754-BLSA 5754, OL, E

T: top (impacted); B: bottom; HS: high strength; LS: low strength; A: adherend; OL: overlap length (b); E: impact energy (E).

For the same adhesive joints and test conditions, increasing the overlap length to 40 mm improves the overall dynamic bending stiffness of adhesive joints; the contact force levels increase partly and the total contact durations are not affected apparently (Figure 5). This improvement in the overall bending stiffness reduces the deformation speed of the adhesive layer, and the adhesive joint can withstand properly the transferred impact energy by the top adherend. Al 5754 adherend(s) also improve the plastic dissipation capability of the adhesive joint to impact energy levels in comparison to Al 2024 adherends. As a result, whatever the impact energy or the overlap length is, the presence of an adherend with good plastic deformation capability improves the overall plastic dissipation capability of the adhesively bonded single-lap joints; therefore, the adhesive layer experiences lower deformation energy.

Figure 6 shows the effects of the impact energy level, overlap length, and adherend material combination on the contact force-central deflection variations based on the experimental and numerical results for adhesive single-lap joints. For an overlap length ($b = 25$ mm), the mechanical properties of the top and bottom adherends affect the peak contact force level and the central deflection for impact energy ($E = 3$ J); thus, T 2024-B 2024 adhesive joint experiences higher contact forces; T 2024-B 5754, T 5754-B 2024, and T 5754-B 5754 adhesive joints follow, respectively (Table 3). Al 2024 adherend improves the overall bending stiffness of the adhesive lap joint; consequently, the contact force levels increase whereas the central deflections decrease. The highest central deflections and the lowest load levels occur in T 5754-B 5754 adhesive joints. Both T 2024-B 5754 and T 2024-B 2024 adhesive joints exhibit a better bending stiffness; thus, higher contact forces and lower central deflections occur. Al 5754 allows the adhesive joint to gain a better plastic deformation capability since Al 5754 adherend can deform plastically and dissipate impact energy well (E^d, Table 3). The position of Al 5754 adherend appears as an important parameter; thus, a top Al 5754 adherend decreases contact force levels moderately in comparison to those in T 2024-B 5754 adhesive joint, and the central deflections decrease negligibly. A better plastic deformation capability of adherend material results in the adhesive layer experiencing lower energy levels transferred by the top adherend. Increasing the impact energy to 11 J makes the contact force levels and the central deflections more apparent (Figure 6, Table 3). Similar and dissimilar adhesive joints reflect partly or full failures in the adhesive layer. The plastic deformation capability of adherends affects the bending impact behaviour of adhesive single-lap joints similarly. The presence of Al 2024 adherend, especially as a top adherend, improves the overall bending stiffness of the adhesive joint; the contact force levels increase whilst the permanent central deflections decrease. However, this causes the adhesive layer to face larger impact energy, and a larger damage region in the adhesive layer or full failure appears. On the contrary, an Al 5754 top adherend reduces the impact force levels and the permanent central deflections increase due to apparent plastic deformations in Al 5754 adherends. Therefore, full damage is not observed in the adhesive layer; the most region of the adhesive layer still holds adherends together (Table 3). Increasing the overlap length to 40 mm improves the overall dynamic bending stiffness of adhesive joints; the contact force levels increase and the permanent central deflections decrease partly (Figure 6). A larger adhesive bonding region improves the load-carrying capability of similar and dissimilar

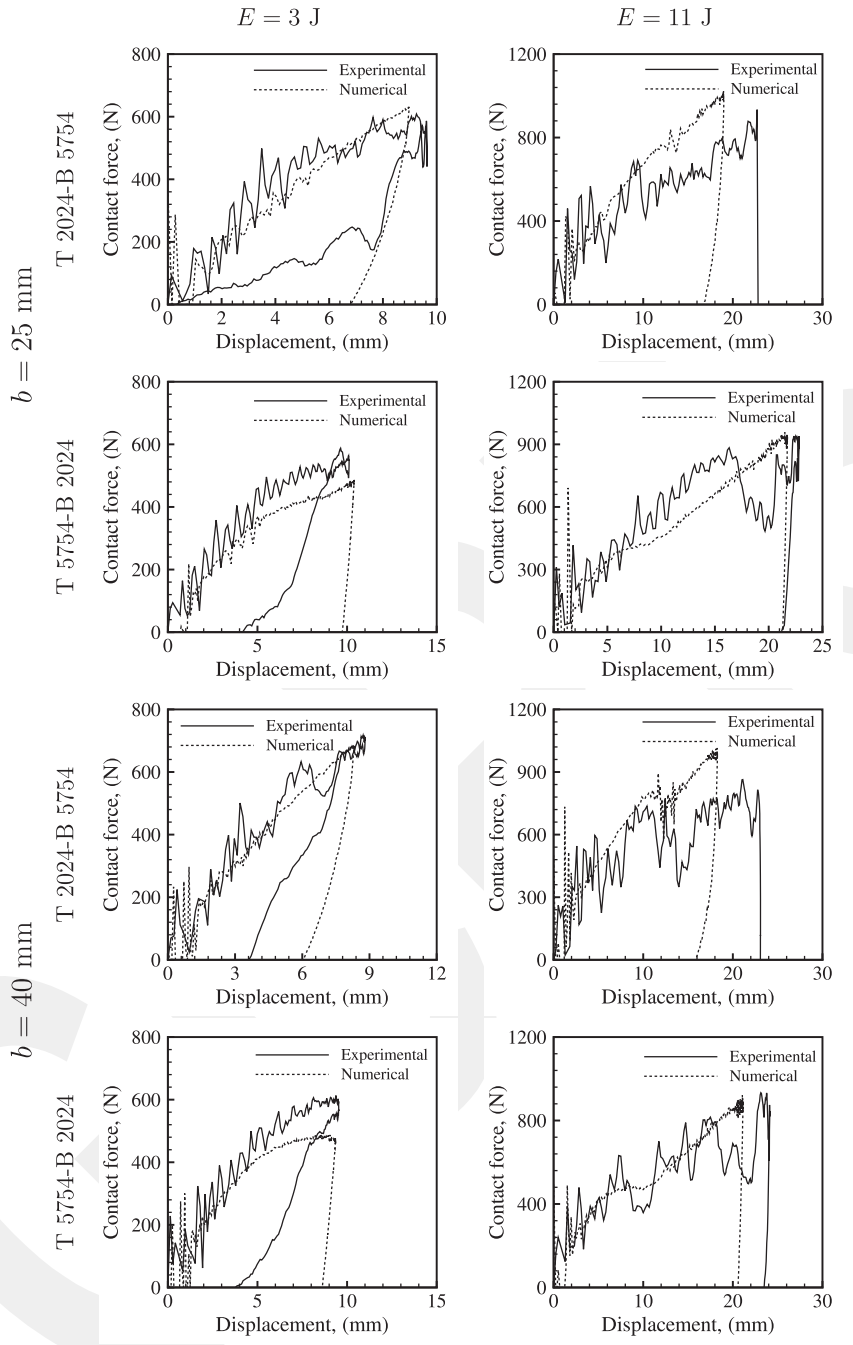

Figure 6. Experimental and numerical contact force-central deflection diagrams for dissimilar adhesive single-lap joints ($b = 25$, 40 mm, $E = 3$, 11 J).

adhesive single-lap joints. The plastic deformations experienced by both adherends reduce since a larger adhesive layer contributes to the dissipation of impact energy. However, a better plastic deformation capability for adherends results in a better

dissipation of impact energy for adhesively bonded single-lap joints, lower contact force levels, and larger permanent central deflections to occur.

In the low-velocity impact tests and explicit finite element analyses of dissimilar adhesively bonded single lap joints three stages are observed in essence (Figures 5, 6): (i) the onset of contact between the impactor and top adherend, damage does not occur, (ii) plastic deformations initiate to occur in both adhesive and adherends, the adhesive layer begins to undergo damage, the contact force initiates to oscillate. As the contact force becomes peak the oscillated force reaches maximum which is an indication of severe damage formation, and (iii) the impactor rebounds while the adhesive joint is still under dynamic excitation, and the contact force tends to decrease towards zero. In the three point-bending impact tests the edges of lower and upper adherends around the supports are free in general. Therefore, any in-plane internal force is not exerted as the adhesive lap joint continues to deflect transversely. In the present study, the edges of upper and lower adherends were fixed, this causes an internal force acting in the in-plane of adhesive lap joints as they deflect transversely. This makes the adhesive joints stiffer to bending, a stress-stiffening state occurs; therefore, the higher contact force formation appears. As a result, the in-plane stress and strain states of adhesive and adherends are affected. A stiffer structure tends to oscillation more, and the contact force is sensitive to oscillations. This is thought to be the main reason for apparent oscillations in experimental force-time and force-deflection diagrams. Secondly, the internal damage mechanism affects certainly the contact force variations since the bending stiffness decreases with increasing internal damage, and the overall load-carrying capability of the adhesive joints gets lost gradually (Figure 11). Thus, as the adhesive damage propagates gradually, the connection of adhesive and adherend disappears and the stored elastic energy in adherends is restored and a spring-back incident is observed more apparently in the transverse plane. This reflects also on the contact force and transverse deflection variations as oscillations. For lower impact energy of 3 J the main characteristics of experimental and numerical contact force-time variations are very close whilst the apparent oscillations are observed in the contact force-deflection diagrams (Figures 5, 6). Larger impact energy of 11 J resulted in more apparent oscillations, the damage was initiated earlier and propagated faster. Therefore, the period of oscillations gets narrower whilst their amplitudes get larger due to the spring-back behaviour of adherends as a result the elastic energy in adherends is released more often. In addition, the adhesive damage modes change due to spring-back behaviour; the adhesive (interfacial) or cohesive damage occurs (Figure 11). Thus, the maximum principal direction of the stress state at the free end of the damaged adhesive determines the adhesive damage type (excluding other parameters and imperfect bonding) after the spring-back is completed and the impactor continues to penetrate. In the explicit finite element model, the damage evaluation and softening rules were implemented for both adherends and adhesives. For the adherend materials and adhesive (continuum part), the piece-wise elasto-plastic material approach was implemented, the failure was predicted based on the failure strain and the failed elements were degraded with a linear softening rule in order not to cause instability in time integration due to sudden stiffness loses. A cohesive model was applied for adhesive interfaces and similar damage evaluation and softening rules according to the cohesive

model were applied for similar reasons. Sudden stiffness changes due to the failed element result in instability in the time integration; therefore, many viscous parameters are used in Abaqus software to smooth the solution stages for the local regions whose mechanical characteristics are suddenly changed and for especially time integration with finite difference approach. Consequently, the effect of stiffness changes as oscillations is rarely apparent in the explicit finite element analyses. However, the correctly performed experiments reflect the actual behavior of the structures.

After the impact tests of dissimilar adhesive single-lap joints, the permanent central deflections (δ) at the overlap region and the axial separation length (Δ) of the adhesive layer, which indicates damage initiation and propagation, were measured from the permanently deformed geometries of the adhesive joints (Figure 7). These experimental values were compared with those obtained from the explicit finite element analyses to determine the accuracy and validity of the present finite element model, especially for the adhesive region. In addition, the effects of overlap length, impact energy, and adherend material combination on the bending impact response of adhesively bonded single-lap joint was investigated.

Figure 7 compares the measured (E) and calculated (N) permanently deformed geometries of dissimilar adhesive single-lap joints with the permanent central deflections ($\delta_{N,E}$) and axial separation lengths ($\Delta_{N,E}$). For both overlap lengths and impact energy levels, the adhesive failure initiates at the right free end of the top adherend-adhesive interface close to the top adherend and propagates along with this top adherend-adhesive interface. There is a good agreement between the experimental and predicted permanent central deflections and axial separation lengths. For $b = 25$ mm and $E = 3$ J the presence of Al 2024 adherend increases the overall bending stiffness of the adhesive joint, and the central permanent deflections decrease. Any adhesive failure initiation and propagation were not observed for T 2024-B 5754 and T 2024-B 2024 adhesive joints whereas T 5754-B 2024 and T 5754-B 5754 adhesive joints undergo adhesive failure along with the top adherend-adhesive interface (Table 3). The predicted and measured permanent central deflections and axial separation lengths are close reasonably, and both experimental and predicted after-impact deformed geometries of dissimilar adhesive single-lap joints are similar. Al 2024 adherends do not exhibit apparent plastic deformations whereas Al 5754 adherends undergo considerable plastic deformations. The measured and calculated permanent central deflections are higher for T 5754-B 2024 and T 5754-B 5754 adhesive joints ($E = 3$ J).

The adhesive lap joints with Al 2024 adherends have a larger bending stiffness, but this results in the adhesive layer undergoing higher contact forces, and to tend an earlier failure. This becomes more apparent for $E = 11$ J (Figure 7); thus, the present adhesive joint configurations undergo full or partly adhesive failure. The permanent central deflections increase. Both T 2024-B 5754 and T 2024-B 2024 adhesive joints fail completely whereas T 5754-B 2024 and T 5754-B 5754 adhesive joints fail partly (Table 3). Al 2024 adherends improve the overall bending stiffness and cause the adhesive layer to fail earlier stages of the impact load. However, Al 5754 adherends improve the plastic dissipation capability (E^d) of the adhesive single-lap joint against the applied impact energy. Consequently, the adhesive layer experiences a lower portion of impact energy and the remaining undamaged adhesive region can still withstand the remaining

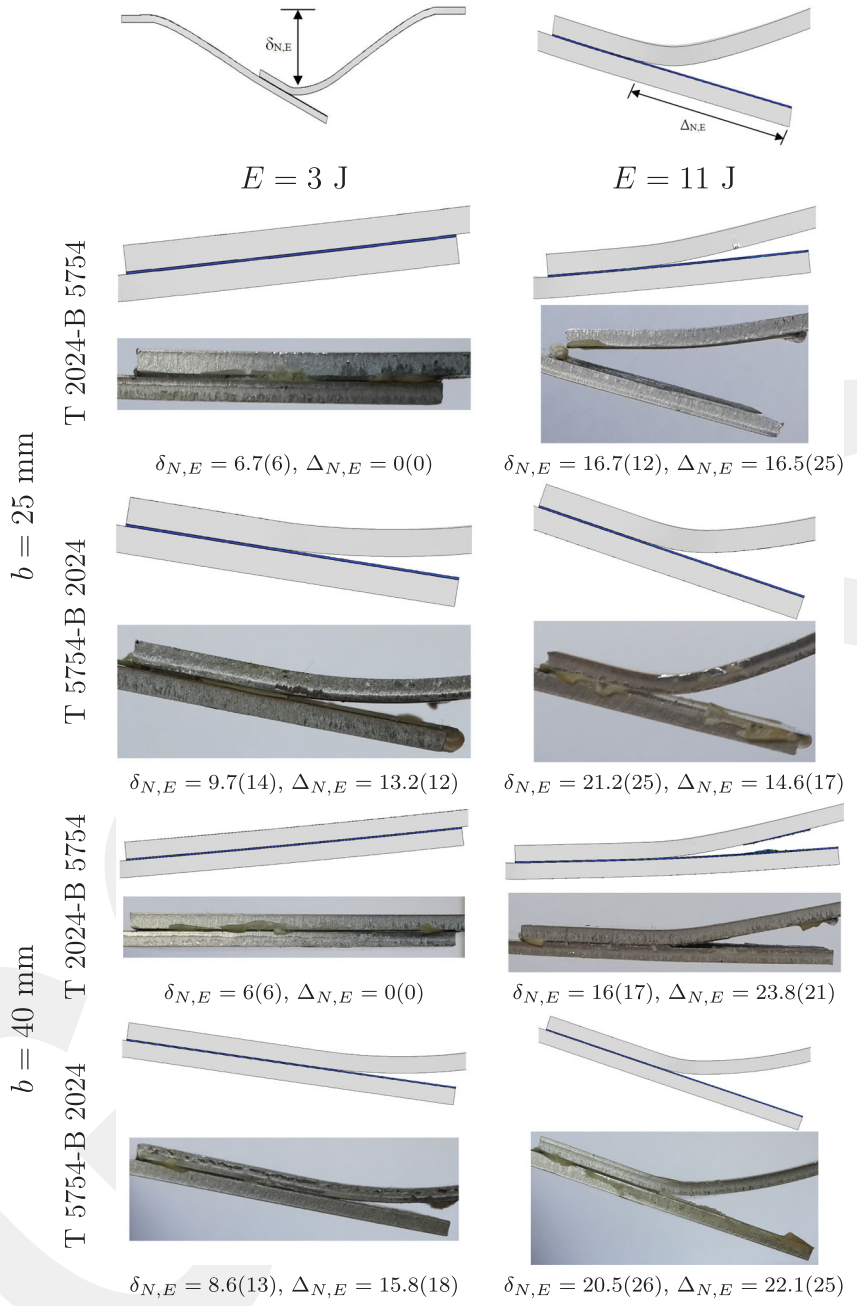

Figure 7. Experimental (E) and predicted (N) after-impact deformed geometries of the overlap region of dissimilar adhesive single-lap joints ($b = 25$, 40 mm, $E = 3$, 11 J, units in mm).

impact energy. In addition, a top Al 5754 adherend improves the plastic energy dissipation capability (E^d) of dissimilar adhesive joints (Table 3). Both permanent central deflections and axial separation lengths of the T 5754-B 2024 adhesive joint are lower than those of T 5754-B 5754 adhesive joints. For $b = 25$ mm and $E = 3$ J, the ratio of the axial separation length to the overlap length (Δ/b) becomes 0, 0.48, 0, and 0.4 for

T 2024-B 5754, T 5754-B 2024, T 2024-B 2024, and T 5754-B 5754 adhesive joints, respectively whereas for $E = 11$ J, they are 1, 0.68, 1, and 0.72, respectively. Two Al 5754 adherends or an Al 5754 top adherend in the adhesive single-lap joint results in adhesive failure but Al 5754 adherends can dissipate impact energy and can slow down failure propagation along with the adhesive interface especially for a high impact energy ($E = 11$ J).

Increasing the overlap length improves the overall bending stiffness of adhesive joints (Table 3); the central permanent deflections decrease for a low impact energy ($E = 3$ J) but this effect becomes small for a high impact energy ($E = 11$ J). All adhesive joint configurations exhibit a partial failure through the adhesive layer except T 2024-B 5754 adhesive joints ($E = 3$ J). Similar partial adhesive failure formations appear for $E = 11$ J whilst T 2024-B 2024 adhesive joint fails completely. For $b = 40$ mm and $E = 3$ J, the ratio of the axial separation length to the overlap length (Δ/b) becomes 0, 0.45, 0.45, and 0.425 for T 2024-B 5754, T 5754-B 2024, T 2024-B 2024, and T 5754-B 5754 adhesive joints, respectively whereas for $E = 11$ J, they are 0.525, 0.625, 1.0, and 0.50, respectively. Increasing impact energy results in a larger axial separation. A larger overlap length provides a bonding area that can dissipate more amount of impact energy in comparison to a joint with a shorter overlap length. Thus, increasing overlap length as well as bonding area provide a lower averaged shear stress distribution and contributes to the bending stiffness of the overlap region. As the rotation of the overlap region decreases with increasing overlap length the effects of out-plane loads on the adhesive-free edges, such as peeling stresses, can be relieved and the adhesive layer undergoes a stress state that the shear stresses are more uniform whilst the normal (peeling) stresses get lower. A larger bonding (ductile) area can dissipate a larger amount of impact energy. This benefit from increasing the ratio of overlap length/overall joint length is limited to a specific ratio depending on the loading and boundary conditions, adhesive joint configuration [28–33]. Two Al 5754 adherends or an Al 5754 top adherend can slow down failure propagation along with the adhesive interface.

Figures 8, 9 show the damage initiation and propagation through the adhesive layer of dissimilar adhesive single-lap joints for impact energies ($E = 3$, 11 J) and overlap lengths ($b = 25$, 40 mm), respectively. Explicit finite element analyses showed that the adhesive damage initiated at the right free edge of the top adherend-adhesive interface and propagated along with this adhesive interface for dissimilar adhesive single-lap joints. Therefore, the in-plane damage distributions through the top cohesive region representing the top adherend-adhesive interface are plotted for both two impact energies and two overlap lengths. This was repeated for each of the dissimilar adhesive single-lap joints. As seen from the colour bar at the top, grey and blue colours indicate failed adhesive regions and healthy adhesive regions which can still carry the load, respectively. The colour ranges between blue and grey colours show damage levels with a damage index varying between lower and upper limits of 0 and 1.0. The damage regions were plotted at different impact stages. For an overlap length ($b = 25$ mm), the adhesive damage propagates faster comparatively through the middle regions of the top adhesive interface whilst it propagates partly slower near the side edges of the in-plane top interface due to Poisson's effect of bi-material interface and free edges

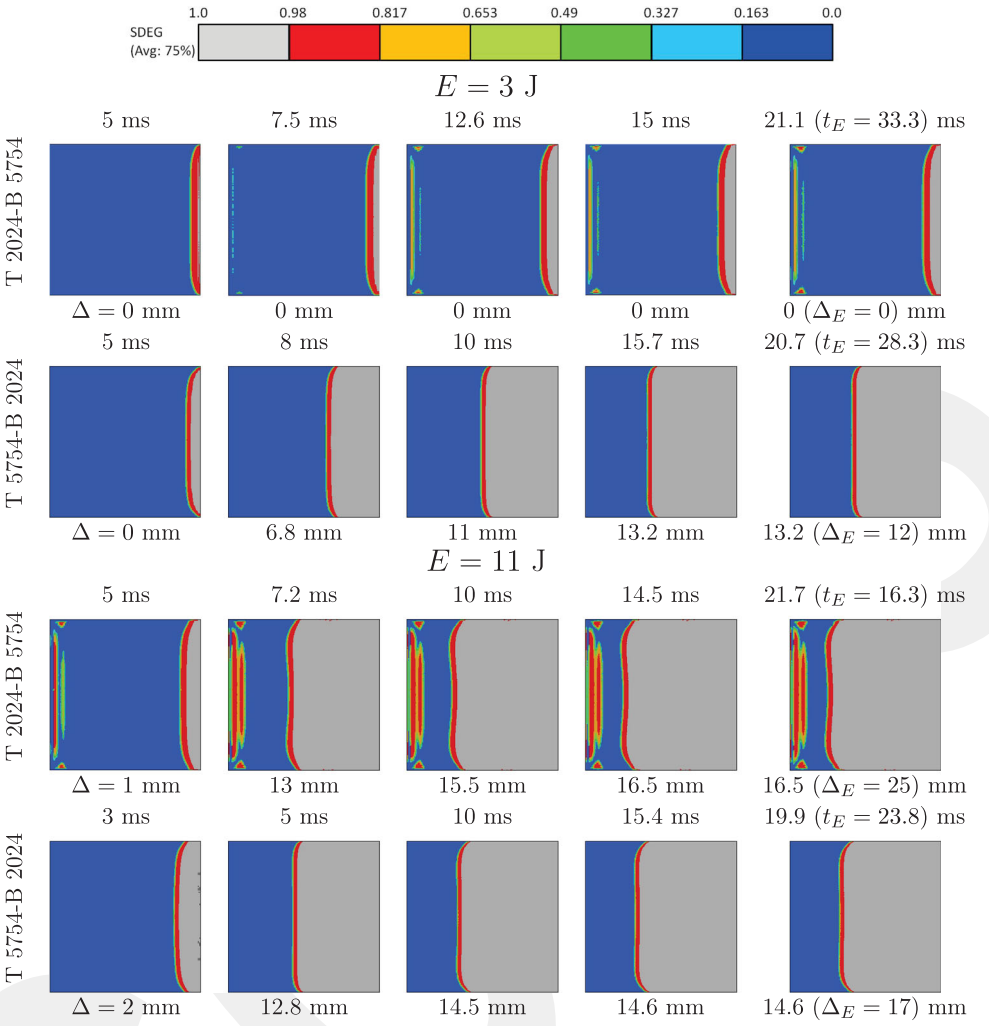

Figure 8. Damage initiation and propagation in dissimilar adhesive single-lap joints ($b = 25$ mm, $E = 3$ and 11 J).

conditions (Figure 8). T 2024-B 5754 adhesive joint also exhibits damage initiation and propagation from the left free edge of the top adherend-adhesive interface. The damage spreads over a larger to smaller area in the adhesive layers of T 2024-B 2024, T 5754-B 2024, T 5754-B 5754, and T 2024-B 2024 adhesive joints in sequence ($E = 3$ J, Table 3). Increasing the impact energy ($E = 11$ J) results in damaged adhesive regions increase whereas the damage initiation and propagation through the adhesive layer appear in a similar mechanism to ($E = 3$ J). T 2024-B 2024 and T 2024-B 5754 adhesive joints experience full damage in the adhesive layer whereas other joint configurations exhibit partial damage propagation through the top adherend-adhesive interface. The damage spreads over a larger to smaller area in the adhesive layer of T 5754-B 5754 and T 5754-B 2024 adhesive joints in sequence ($E = 11$ J). Al 2024 adherend improves the overall bending stiffness; however, this causes the adhesive layer to experience a larger portion of impact energy, and the adhesive layer tends to damage earlier in a larger

region. The plastic deformation capability of Al 5754 adherend reduces the portion of impact energy to be transferred to the adhesive layer. Especially, an Al 5754 top adherend contributes to the load carrying and impact energy-absorbing capabilities of the dissimilar adhesive single-lap joints *vs.* the bending impact loads.

Increasing the overlap length ($b = 40$ mm) does not affect the mechanism of the damage initiation and propagation in the adhesive layer; thus, the damage initiates at the right free edge of the top adherend-adhesive interface and propagates along with the top adhesive interface for both impact energy levels (Figure 9). However, T 2024-B 5754 adhesive joint also experiences the initiation and propagation from the left free edge of the top adherend-adhesive interface at the advancing stages of the penetration of the impactor. The damage spreads over a larger to smaller area in the adhesive layers of T 2024-B 2024, T 5754-B 2024, T 5754-B 5754, and T 2024-B 5754 adhesive joints in sequence ($E = 3$ J, Table 3). The effect of a larger overlap length becomes more apparent for impact energy ($E = 11$ J). All adhesive joints can withstand the applied impact energy except for T 2024-B 2024 adhesive joint. Similarly, the damage spreads over a larger to smaller area in the adhesive layer of T 2024-B 2024, T 5754-B 2024, T 5754-B 5754, and T 2024-B 5754 adhesive joints in sequence ($E = 11$ J). Al 2024 adherends improve the bending stiffness of the adhesive joint but increase induced contact forces and the portion of impact energy transferred to the adhesive layer. Consequently, the adhesive layer tends to damage formation earlier. Al 5754 adherends improve the impact energy dissipation capability of similar and dissimilar adhesive

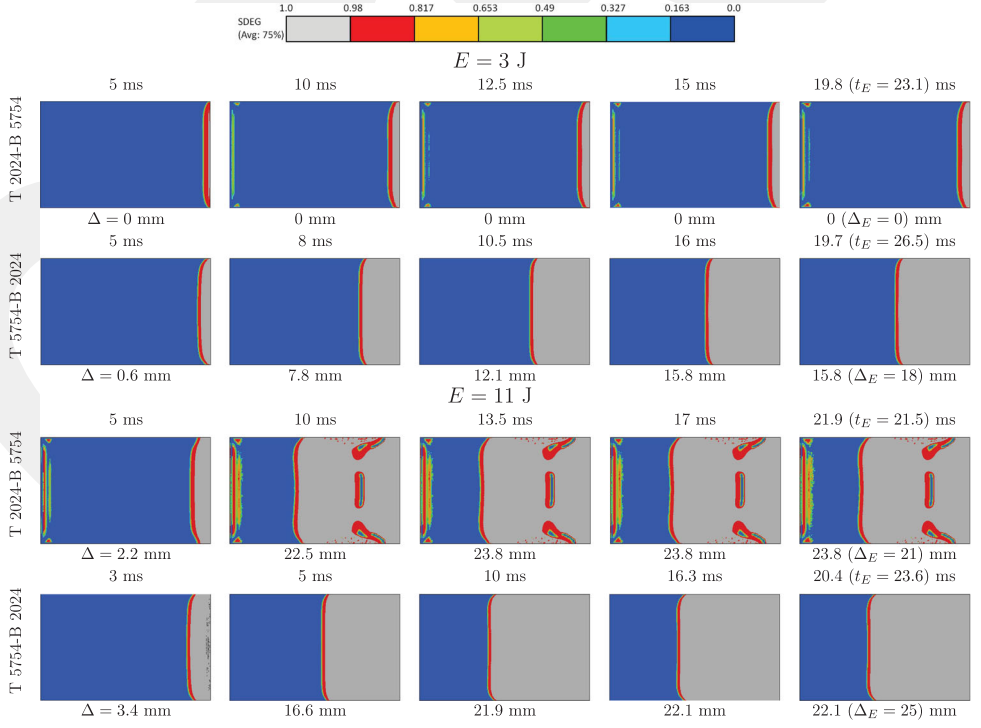

Figure 9. Damage initiation and propagation in dissimilar adhesive single-lap joints ($b = 40$ mm, $E = 3$ and 11 J).

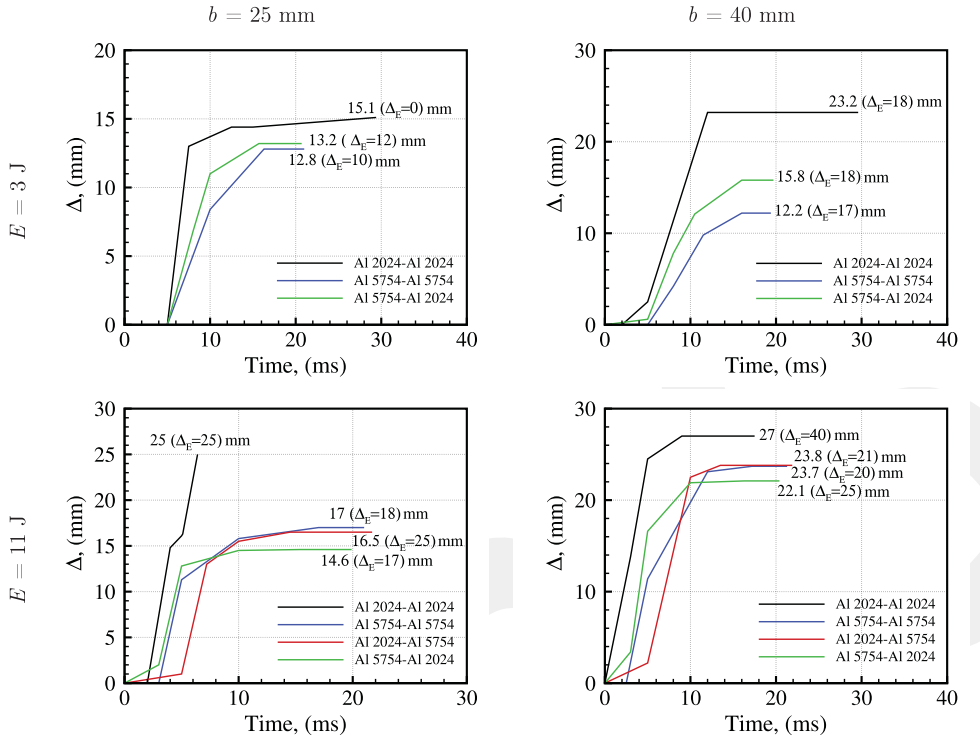

Figure 10. Effects of overlap length and impact energy on the axial separation (Δ) variations *vs.* time for similar and dissimilar adhesive single-lap joints [17].

joints. A top Al 5754 adherend (5754-B 2024) improves these capabilities additionally. A large overlap length provides a large bonding area, and this relieves shear stress distributions over the adhesive layer and improves the dynamic load-carrying capability of the adhesive single-lap joints.

A 3D cohesive zone model for the upper and lower adherend-adhesive interfaces and the meso-level continuum approach for the adhesive region between these two interfaces are reasonably successful to predict the damage initiation and propagation in the adhesive layer. The predicted axial separation lengths, permanent central deflections, the damage initiation and propagation mechanism and locations in the adhesive layer, the shape and size of the damaged adhesive regions, the after-impact deformed geometries of both adherends are similar to experimental ones, and the numerical and experimental results are consistent.

As the impact energy is increased the deformation rates of aluminium adherends and the adhesive layer can play an important role in the dynamic deformation response of the adhesive single-lap joints under a bending impact load. A simple evaluation can be made for the damage propagation speed to analyse the propagation stages of adhesive damage. To show the effects of impact energy, overlap length, and the plastic deformation capability of adherend materials on the damage propagation speed in the adhesive layer or along the adhesive interfaces, the predicted temporal variations of the axial separation length (Δ) are shown for similar and dissimilar aluminium adhesive single-lap joints (Figure 10). For an overlap length ($b = 25$ mm) and impact energy

($E = 3$ J), T 2024-B 5754 dissimilar adhesive joint does not experience damage in the adhesive layer. T 2024-B 2024 similar adhesive joint exhibits a maximum separation (15.1 mm) which increases sharply in the first 10 ms, reaches a peak contact force level (Figure 10), and varies negligibly. This occurs since Al 2024 adherends with high strength behave stiffer, cannot dissipate properly impact energy, and the adhesive layer subjects to most of the impact energy. Al 5754 adherends can dissipate most of the impact energy; therefore, the damage begins late and propagates slower. The predicted final axial separation lengths become 13.2 and 12.9 mm for T 5754-B 2024 dissimilar and T 5754-B 5754 similar adhesive single-lap joints, respectively. Increasing the impact energy ($E = 11$ J) results in the axial separation lengths increasing. All similar and dissimilar aluminium adhesive single-lap joints experience partial or full adhesive damage. T 2024-B 2024 similar adhesive joint reflects the fastest damage propagation in the adhesive layer. An apparent impact energy dissipation is not observed. T 5754-B 5754 similar and T 2024-B 5754 dissimilar adhesive joints have similar damage initiation and propagation behaviour as well as the final separation speeds. These two adhesive single-lap joints exhibit apparent impact energy dissipation and evidently slow damage propagation speeds. However, T 5754-B 2024 dissimilar adhesive joint has a better impact energy dissipation capability. Thus, it exhibits a fast damage initiation and propagation until the contact force becomes peak (Figure 10), and then the damage propagation in the adhesive layer becomes negligible, Al 5754 top adherend dissipates most of the impact energy. As the impact energy is increased the earlier stages of the damage propagation in the adhesive layer occur at high speeds, the plastic deformation capability of adherends becomes more apparent until the peak contact force is reached; thus, the stored elastic energy is restored by the joint members.

Increasing overlap length ($b = 40$ mm) does not affect apparently the variations of axial separation *vs.* time for similar and dissimilar adhesive joints. A fast damage propagation occurs in the adhesive layer until the peak contact force level is reached, and then the damage propagation becomes negligible. Al 5754 adherend can still dissipate impact energy properly due to its relatively low strength and better plastic deformation capability. Therefore, the damage in the adhesive layer of dissimilar adhesive joints occurs late and propagates slower. As a result, increasing overlap length improves the overall bending stiffness of adhesive joints; therefore, it is expected that the peeling stresses are reduced whereas the shear stress remains almost the same in the case of quasi-static loadings. However, a stiffer overlap region under an impact loading results in the adherends gaining bending stiffness and rarely to tend plastic deformations. Consequently, the adhesive layer imposes a larger portion of the impact energy. This appears as a larger adhesive damage region and slower failure propagation.

Figure 11 shows the fracture surfaces of the top and bottom adherends of dissimilar aluminium adhesive single-lap joints having overlap lengths ($b = 25$, 40 mm) for different impact energies ($E = 3$, 11 J). The failure mode types of adhesive single-lap joints were also summarized in Table 3. The grey bars indicate the final axial separation distance of damaged adhesive regions for each specimen. Some adhesive joints did not fail completely; therefore, these specimens were forced to separate by applying force by hand to examine the characteristics of the fracture surfaces during the impact tests.

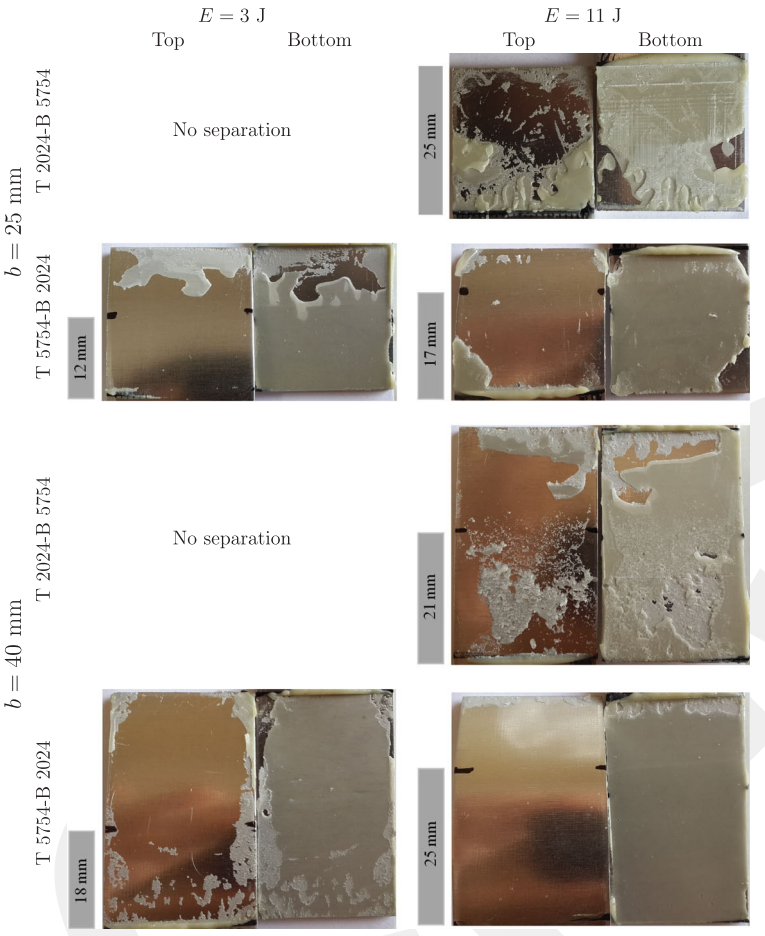

Figure 11. Fracture surfaces of the top and bottom adherends of dissimilar adhesive single-lap joints ($b = 25$, 40 mm and $E = 3$, 11 J).

The fracture surfaces of similar adhesive single-lap joints were given in Ref. [16], these fracture surfaces were evaluated and summarized in Table 3. In case of an overlap length ($b = 25$ mm), T 2024-B 2024 similar and T 2024-B 5754 dissimilar adhesive joints did not fail completely through the adhesive layer for impact energy ($E = 3$ J) (Figure 11, Table 3). In general, the adhesive failure initiates at the right free edge of the top adherend-adhesive interface and propagates along with this top adherend-adhesive interface. T 5754-B 2024 dissimilar and T 5754-B 5754 similar adhesive joints failed partly and have blank surfaces at a certain axial distance on their top adherends, which indicates an interfacial failure. T 5754-B 5754 similar adhesive joint exhibits comparatively a smaller fracture surface. Al 5754 adherends can dissipate impact energy properly, and the adhesive layer can damage less. In case impact energy ($E = 11$ J), T 2024-B 2024 similar and T 2024-B 5754 dissimilar adhesive joints fail completely. The failure initiates at the right free edge of the top adherend-adhesive interface and propagates along with this interface. However, in the vicinity of the left edge of the overlap region an adhesive failure mode occurs since there is not enough bonding area that may withstand the applied impact load. In T 2024-B 5754 dissimilar

adhesive joint the adhesive damage initiates at the right free edge of the top adherend-adhesive interface, and propagates in both interfacial and adhesive failure modes until the nearly half axial distance of the overlap length, and then returns the interfacial adhesive failure mode and propagates in this mode. T 5754-B 2024 dissimilar and T 5754-B 5754 similar adhesive joints incur an interfacial failure propagation until a specific axial distance along with the top adherend-adhesive interface which initiates at the right free edge of this interface. The adhesive layer has partial damage for these joints, Al 5754 adherends can dissipate impact energy; consequently, the adhesive failure can be reduced. Especially, an Al 5754 top adherend in the dissimilar adhesive single-lap joint can improve additionally the impact energy-dissipation capability of the adhesive joint.

Increasing an overlap length ($b = 40$ mm) improves the load-carrying capability of the adhesive joint *vs.* the bending impact load (Figure 11) since the overall bending stiffness of the adhesive single-lap joint increases and the rotation of the overlap region reduces. Consequently, the peeling stress reduces at the free edges of the adhesive layer, the adhesive layer tends to deform mostly in shear. T 2024-B 5754 dissimilar adhesive joint does not experience adhesive failure for impact energy ($E = 3$ J). T 5754-B 2024 dissimilar and T 5754-B 5754 similar adhesive joints experience failure which initiates at the right free edge of the top adherend-adhesive interface and propagates along with the top adhesive interface. T 5754-B 2024 dissimilar adhesive joint has also some small adhesive residues over the fracture surface of the top Al 5754 adherend; consequently, the failure mechanism is mostly interfacial, but cohesive failure appears around the side free edges of the fracture surface. T 2024-B 2024 similar adhesive joint sustains a dominant cohesive failure near the top adherend-adhesive interface (Table 3). A larger overlap region provides the adhesive layer to be able to withstand the impact energy transferred by the top adherend. Increasing the impact energy ($E = 11$ J) resulted in T 2024-B 2024 similar adhesive joint to fail completely in both interfacial and cohesive failure modes and T 5754-B 2024 dissimilar adhesive joint to experience partial failure along with the top adherend-adhesive interface. However, T 2024-B 5754 dissimilar and T 5754-B 5754 similar adhesive joints undergo failure in both largely interfacial and cohesive failure modes. In particular, the mechanical properties of both adherends affect evidently the failure mechanism of the adhesive bonding region. As the adherends become stiffer the cohesive failure appears dominantly whereas the dominant failure mechanism becomes interfacial for the adherends with plastic deformation capability.

Based on the predicted (EFEA, Explicit Finite Element Analysis) damage initiation and propagation in dissimilar adhesive single-lap joints (Figures 8, 9) and the fracture surfaces of the top and bottom adherends after the impact tests (Figure 11) it was observed that (i) the damage initiation (EFEA) appeared at the free edge of the top adherend (impacted)-adhesive interface, propagated along with this interface for all joint configurations and impact energy levels (Figures 8, 9). Experimental fracture surfaces appeared mostly in adhesive (interfacial) failure mode along the top adherend (impacted)-adhesive interface. However, for T 2024-B 5754 joint under a higher impact energy (11 J) adhesive impurities on the top adherend surface were observed, which indicates partly thin cohesive failure close to the top adhesive interface. In the finite

element model of the adhesive layer, the cohesive elements only give nominal stresses in an artificial volume whilst the continuum elements are capable of calculating three-dimensional stress and strain states. Therefore, the maximum principal and shear directions cannot be determined suitably; therefore, the probable direction of damage propagation remains through the path of cohesive elements and does not directly into the adhesive region consisted of continuum elements depending on the stress state. Unfortunately, the cohesive elements are not compatible with the continuum elements as expected. (ii) Predicted and experimental axial separation lengths were very close; thus, (Δ_N, Δ_E): $(0,0)^{25,3}$, $(13.2,12)^{25,3}$, $(16.5,25)^{25,11}$, $(14.6,17)^{25,11}$ mm (Figures 8, 11) and $(0,0)^{40,3}$, $(15.8,18)^{40,3}$, $(23.8,21)^{40,11}$, $(22.1,25)^{40,11}$ mm (Figures 9, 11) for T 2024-B 5754 and T 5754-B 2024, respectively. The proposed finite element model for adhesive layer and adherend can predict the damage initiation and propagation reasonably. (iii) T(op) 5754 (impacted) adherends for impact energies of 3 and 11 J exhibit considerable plastic deformations and dissipate more impact energy (Figure 7) in comparison to T 2024 adherends. However, this causes significant rotations in the overlap region and peeling stress to become more apparent. Consequently, axial separation lengths or damage propagation are longer in adhesive joints with T 5754 (impacted) adherends. EFEA and experimental results are conformable reasonably in this respect (Figures 7–9, 11).

Based on the macroscope photographs of the fracture surfaces (Figure 11) the adhesive residues on the fracture surface of the top adherend become more apparent for T

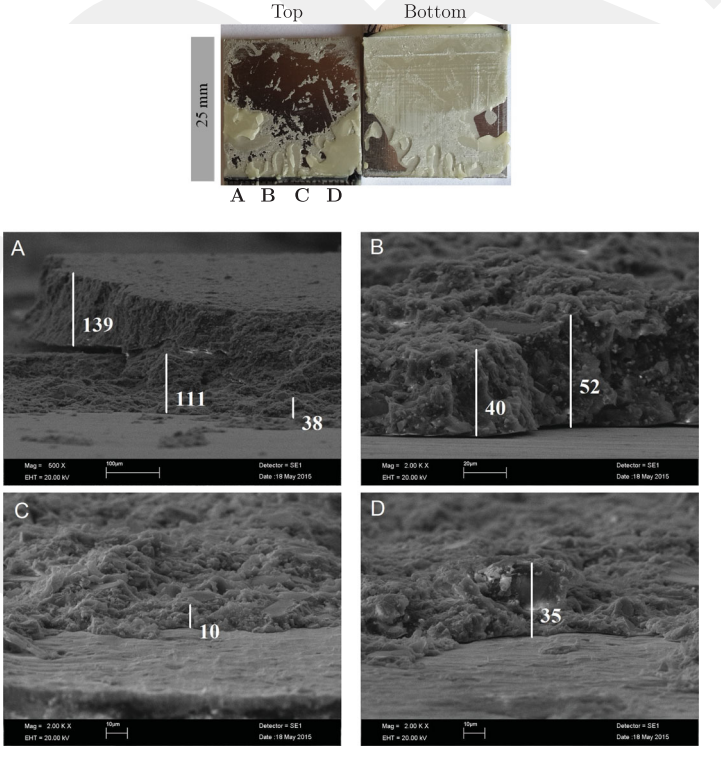

Figure 12. SEM photographs of adhesive fracture surfaces around the adhesive-free edges of dissimilar (Al 2024-Al 5754) adhesive single-lap joints ($b = 25$ mm and $E = 11$ J, measurements in μm).

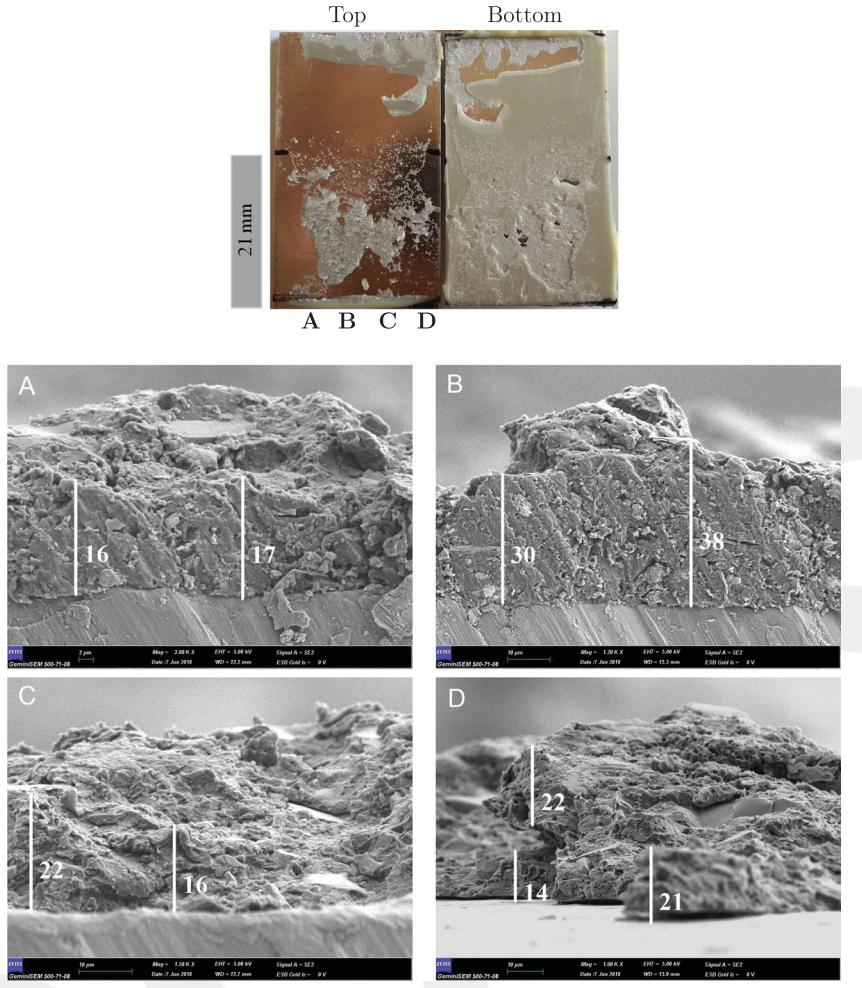

Figure 13. SEM photographs of adhesive fracture surfaces around the adhesive-free edges of dissimilar (Al 2024-Al 5754) adhesive single-lap joints ($b = 40$ mm and $E = 11$ J, measurements in μm).

2024-B 2024 similar and T 2024-B 5754 dissimilar adhesive joints ($E = 11$ J, Ref. [16]). Figures 12, 13 show the scanning electron microscope (SEM) photographs of adhesive residues taken at the locations (A, B, C, and D) along the adhesive right free edge of T 2024-B 5754 dissimilar adhesive single-lap joints ($b = 25$ and 40 mm, $E = 11$ J), respectively. The failure occurs first in cohesive mode near the top adherend along the right free edge of the adhesive layer. The thickness of adhesive residues changes among 13–140 μm at different locations ($b = 25$ mm, Figure 12). The adhesive residues have a larger thickness near the side edges of the adhesive layer (A,D) and reduce towards the middle region of the adhesive layer. The free edges experience zero shear stress conditions and Poisson's effect becomes more apparent. For T 2024-B 5754 dissimilar adhesive joint the thickness of the adhesive residues reduces, but the failure mode is still cohesive. For an overlap length ($b = 40$ mm, Figure 13) the averaged adhesive residue thickness increases for a stiffer T 2024-B 2024 similar adhesive joint [16] whilst T 2024-B 5754 dissimilar adhesive joint has apparently lower adhesive residue thickness.

In case one or both of the top and bottom adherends has a better plastic deformation capability the adhesive joint can dissipate suitably the impact energy, and the adhesive layer undergoes lower impact loads transferred by the top adherend. Stiffer adherends improve the overall bending stiffness of the adhesive joint; however, the adhesive layer experiences higher impact loads since the impact energy cannot be dissipated *via* the plastic deformation of the top adherend. This results in the adhesive bonding region failing dominantly in cohesive failure.

5. Conclusions

This study investigates the effects of adherend strength and plastic deformation capability, overlap length, impact energy on the low speed bending impact behaviour of adhesively bonded dissimilar aluminium single-lap joints. The main findings are as follows:

- Increasing the overlap length or impact energy has an increasing effect on the contact force levels whilst the total contact durations decrease. A large overlap length or stiffer adherend improves the overall bending stiffness of the adhesive single-lap joint. However, this causes higher contact force levels, and the adhesive layer to experience higher impact loads,
- Adherends with a better plastic deformation capability reduce contact force levels and dissipate most of the impact energy by deforming plastically. In case the top adherend of a dissimilar adhesive single-lap joint has a better plastic deformation capability the impact energy dissipation capability of the adhesive joint is additionally improved,
- Similar and dissimilar adhesive single-lap joints exhibited a failure mechanism that initiated at the right free edge of the top adherend-adhesive and propagated along with this top adherend-adhesive interface. For T 2024-B 2024 similar and T 2024-B 5754 dissimilar adhesive single-lap joints the failure initiated at the same location but propagated through the adhesive regions near this top adhesive interface (cohesive failure) whilst this happens only along with the top adhesive interface by leaving a blank surface on the top adherend with negligible adhesive residues for T 5754-B 2024 dissimilar and T 5754-B 5754 similar adhesive single-lap joints. After the damage was initiated it propagated faster in the adhesive single-lap joints with higher bending stiffness. The adhesive damage in the middle region of the adhesive layer propagated faster than in the regions near the side free edges due to Poisson's effect,
- The predicted and experimental contact force-time and contact force-central deflection curves, fracture surfaces were consistent. A 3D-continuum elasto-plastic adhesive layer based on a meso-level damage model between the top and bottom adherend-adhesive interfaces modelled with 3D cohesive laws was reasonably successful to predict through-thickness and interfacial damage initiation and propagation in the adhesive layer.

Acknowledgments

The authors would like to thank the Scientific Research Project Division of Erciyes University under the contract [FYL-2014-5262] for their financial support.

Disclosure statement

No potential conflict of interest was reported by the author(s).

ORCID

M. Kemal Apalak http://orcid.org/0000-0002-3263-5735

References

[1] Adams RD, Comyn J, Wake WC. Structural adhesive joints in engineering. London: Elsevier Applied Science; 1984.
[2] da Silva LFM, Öchsner A, editors. Modeling of adhesively bonded joints. Berlin; Heidelberg: Springer Berlin Heidelberg; 2008.
[3] da Silva LFM, Campilho RDSG. Advances in numerical modelling of adhesive joints. Berlin; Heidelberg: Springer-Verlag; 2012. p. 1–93.
[4] da Silva LFM, Dillard DA, Blackman B, et al. Testing adhesive joints: best practices. Weinheim: John Wiley & Sons; 2012.
[5] Mittal KL. Adhesive joints: formation, characteristics, and testing. New York (NY): Springer Science & Business Media; 2012.
[6] Machado JJM, Marques EAS, da Silva LFM. Adhesives and adhesive joints under impact loadings: an overview. J Adhes. 2018;94(6):421–452.
[7] Higuchi I, Sawa T, Suga H. Three-dimensional finite element analysis of single-lap adhesive joints under impact loads. J Adhes Sci Technol. 2002;16(12):1585–1601.
[8] Sawa T, Suzuki Y, Kido S. Stress analysis and strength estimation of butt adhesive joints of dissimilar hollow cylinders under impact tensile loadings. J Adhes Sci Technol. 2003; 17(7):943–965.
[9] Higuchi I, Sawa T, Okuno H, et al. Three-dimensional finite element analysis of stress response in adhesive butt joints subjected to impact bending moments. J Adhes. 2003; 79(11):1017–1039.
[10] Vaidya UK, Gautam ARS, Hosur M, et al. Experimental–numerical studies of transverse impact response of adhesively bonded lap joints in composite structures. Int J Adhes Adhes. 2006;26(3):184–198.
[11] Yildirim M, Apalak MK. Transverse low-speed impact behavior of adhesively bonded similar and dissimilar clamped plates. J Adhes Sci Technol. 2011;25(1–3):69–91.
[12] Liao L, Sawa T, Huang C. Experimental and FEM studies on mechanical properties of single-lap adhesive joint with dissimilar adherends subjected to impact tensile loadings. Int J Adhes Adhes. 2013;44:91–98.
[13] Asgharifar M, Kong F, Carlson B, et al. Dynamic analysis of adhesively bonded joint under solid projectile impact. Int J Adhes Adhes. 2014;50:17–31.
[14] Yildirim M, Apalak MK. Experimental investigation on transverse low-speed impact behavior of adhesively bonded similar and dissimilar clamped plates. J Adhes Sci Technol. 2014;28(13):1219–1242.
[15] Sankar HR, Adamvalli M, Kulkarni PP, Parameswaran V. Dynamic strength of single lap joints with similar and dissimilar adherends. Int J Adhes Adhes. 2015;56:46–52.
[16] Atahan MG, Apalak MK. Low-speed bending impact behavior of adhesively bonded single-lap joints. J Adhes Sci Technol. 2017;31:1545–1575.

[17] Atahan MG, Apalak MK. Low-speed oblique impact behavior of adhesively bonded single-lap joints. J Adhes Sci Technol. 2020;34(3):263–298.
[18] Boling H, Dongyun G. Dynamic analysis of single-lap, adhesively bonded composite-titanium joints subjected to solid projectile impact. J Adhes Sci Technol. 2018;32(11): 1176–1199.
[19] Machado JJM, Marques EAS, Silva MRG, et al. Numerical study of impact behaviour of mixed adhesive single lap joints for the automotive industry. Int J Adhes Adhes. 2018; 84:92–100.
[20] Jia Z, Yuan G, Feng X, et al. Shear properties of polyurethane ductile adhesive at low temperatures under high strain rate conditions. Compos Part B Eng. 2019;156:292–302.
[21] Jia Z, Yuan G, Feng X, et al. Numerical study on the mechanical behavior of a polyurethane adhesive under high strain rate. Compos Part B Eng. 2019;158:131–140.
[22] Yildiz S, Andreopoulos Y, Jensen RE, et al. Characterization of adhesively bonded aluminum plates subjected to shock-wave loading. Int J Impact Eng. 2019;127:86–99.
[23] Araldite. Epoxy adhesive. Huntsman Advanced Materials; 2015. Available from: http://www.huntsman.com
[24] ABAQUS 6.11. Analysis user's manual, Vol. IV. Elements Dassault Systemes. Available from: http://www.3ds.com
[25] Wong KJ. Moisture absorption characteristics and effects on mechanical behaviour of carbon/epoxy composite: Application to bonded patch repairs of composite structures. Dijon: Université de Bourgogne; 2013.
[26] Campilho RDSG, Banea MD, Neto JABP, et al. Modelling adhesive joints with cohesive zone models: effect of the cohesive law shape of the adhesive layer. Int J Adhes Adhes. 2013;44:48–56.
[27] Camanho PP, Dávila CG. Mixed-mode decohesion finite elements for the simulation of delamination in composite materials. Technical report NASA/TM-2002-211737. Hampton, VA; 2002.
[28] Özel A, Aydin M, Temiż Ş. The effects of overlap length and adherend thickness on the strength of adhesively bonded joints subjected to bending moment. J Adhesion Sci Tech. 2004;18(3):313–325.
[29] Machado JJM, Marques EAS, da Silva LFM. Mechanical behaviour of adhesively bonded composite single lap joints under quasi-static and impact conditions with variation of temperature and overlap. J Composite Mater. 2018;52(26):3621–3635.
[30] Kadioglu F, Avil F, Ercan ME, et al. Effects of different overlap lengths and composite adherend thicknesses on the performance of adhesively-bonded joints under tensile and bending loadings. IOP Conf Ser Mater Sci Eng. 2018;369:012034.
[31] Saeimi Sadigh MA, Paygozar B, da Silva LFM, et al. Creep behaviour and tensile response of adhesively bonded polyethylene joints: single-lap and double-strap. Int J Adhesion Adhesives. 2020;102:102666.
[32] Monteiro J, Salgado RM, da Rocha T, et al. Effect of adhesive type and overlap length on the mechanical resistance of a simple overlap adhesive joint. UPjeng. 2021;7(3):1–12.
[33] Hanumantharaya R, Sogalad I, Basavarajappa S. Investigations on the influence of nano reinforcement on strength of adhesively bonded joints. Mater Today. 2021;45:87–93.